Check for updates

LIMNOLOGY and OCEANOGRAPHY LETTERS

ASLO

Open Access

Limnology and Oceanography Letters 11, 2026, e70086
© 2025 The Author(s). *Limnology and Oceanography Letters* published by Wiley Periodicals LLC on behalf of Association for the Sciences of Limnology and Oceanography.
doi: 10.1002/lol2.70086

LETTER

Imprint of Indian Ocean Dipole on nitrous oxide dynamics

Yangyang Zhao[1*] **Laure Resplandy**[1,2] **Fan Yang**[1] **Xianhui Sean Wan**[3] **Calla M. Marchetti**[4] **Bess Ward**[2]

[1]High Meadows Environmental Institute, Princeton University, Princeton, New Jersey, USA; [2]Department of Geosciences, Princeton University, Princeton, New Jersey, USA; [3]State Key Laboratory of Marine Environmental Science, Xiamen University, Xiamen, China; [4]Program in Atmospheric and Oceanic Sciences, Princeton University, Princeton, New Jersey, USA

Scientific Significance Statement

The northern Indian Ocean emits nitrous oxide (N_2O), a powerful greenhouse gas, to the atmosphere with a strong seasonal cycle driven by monsoon winds and year-to-year variations associated with the natural climate mode called the Indian Ocean Dipole (IOD). However, sparse observations of N_2O in space and time cannot fully capture this temporal variability, leading to potential biases in regional N_2O emissions. We examine the influence of IOD on N_2O seasonality using a regional ocean model over the past four decades. Indian Ocean Dipole imposes a seesaw pattern in N_2O between the western and eastern basin with a stronger response during the positive phases of IOD than during the negative phases. Unfortunately, observational sampling is biased toward regions and IOD phases with lower N_2O levels, likely resulting in the systematic underestimation of N_2O seasonality and N_2O emission estimates. Understanding N_2O seasonal and interannual variability is key to constrain current and future ocean N_2O emissions.

Abstract

The northern Indian Ocean is a hotspot of nitrous oxide (N_2O) emissions, with strong seasonal monsoons and interannual Indian Ocean Dipole (IOD) variability. We examine the IOD influence on N_2O seasonality using a regional ocean model covering 1981–2020, with a focus on the coastal ocean where ΔpN_2O variability is more than threefold greater than in the open ocean. Positive IOD amplifies ΔpN_2O seasonality by a factor 2 to 5 in the east and dampens it by ~ 30% in the west. Negative IOD reverses this pattern but changes are weaker (< 10%). This east/west contrast and asymmetry between positive and negative IOD arise from changes in transport of N_2O produced in subsurface by nitrification and denitrification, and significantly modulate local N_2O emissions (−40% to +130%). Sparse N_2O observations and systematic biases in IOD phase sampling compound seasonal and interannual variability, likely leading to underestimation of N_2O seasonality and emissions in observation-based reconstructions.

The northern Indian Ocean is among the major oceanic emission hotspots of nitrous oxide (N_2O), a powerful greenhouse gas that affects the Earth's climate (Prather 2001; Tian et al. 2020; Yang et al. 2020), and is subject to strong seasonal variations by monsoon winds and significant interannual variations associated with Indian Ocean Dipole (IOD), an analogue of El Niño—

*Correspondence: yangyzhao@princeton.edu

This is an open access article under the terms of the Creative Commons Attribution License, which permits use, distribution and reproduction in any medium, provided the original work is properly cited.

Associate editor: Henrietta Dulai

Southern Oscillation in the tropical Pacific (Vinayachandran et al. 2021; Schott and McCreary 2001; Schott et al. 2009). Observations suggest that the strong N_2O emissions in the northern Indian Ocean undergo a vigorous seasonal cycle, especially in the Arabian Sea (Lal and Patra 1998), increasing by ~ 0.7 Tg N yr^{-1} from the minimum in spring to the maximum in summer (Yang et al. 2020). This increase contributes more than 30% to the seasonal amplitude of global ocean N_2O flux (an increase of ~ 2.2 Tg N yr^{-1} from boreal spring to summer, Yang et al. 2020). However, observation-based estimates of N_2O emissions seasonality are compounded by interannual variability due to sparse and uneven observations in both space and time (Fig. 1a; Supporting Information Fig. S1), leading to biases in ocean N_2O emissions (Tian et al. 2024). For instance, N_2O emissions in the eastern tropical Pacific have been observed to be greatly impacted by El Niño—Southern Oscillation, locally

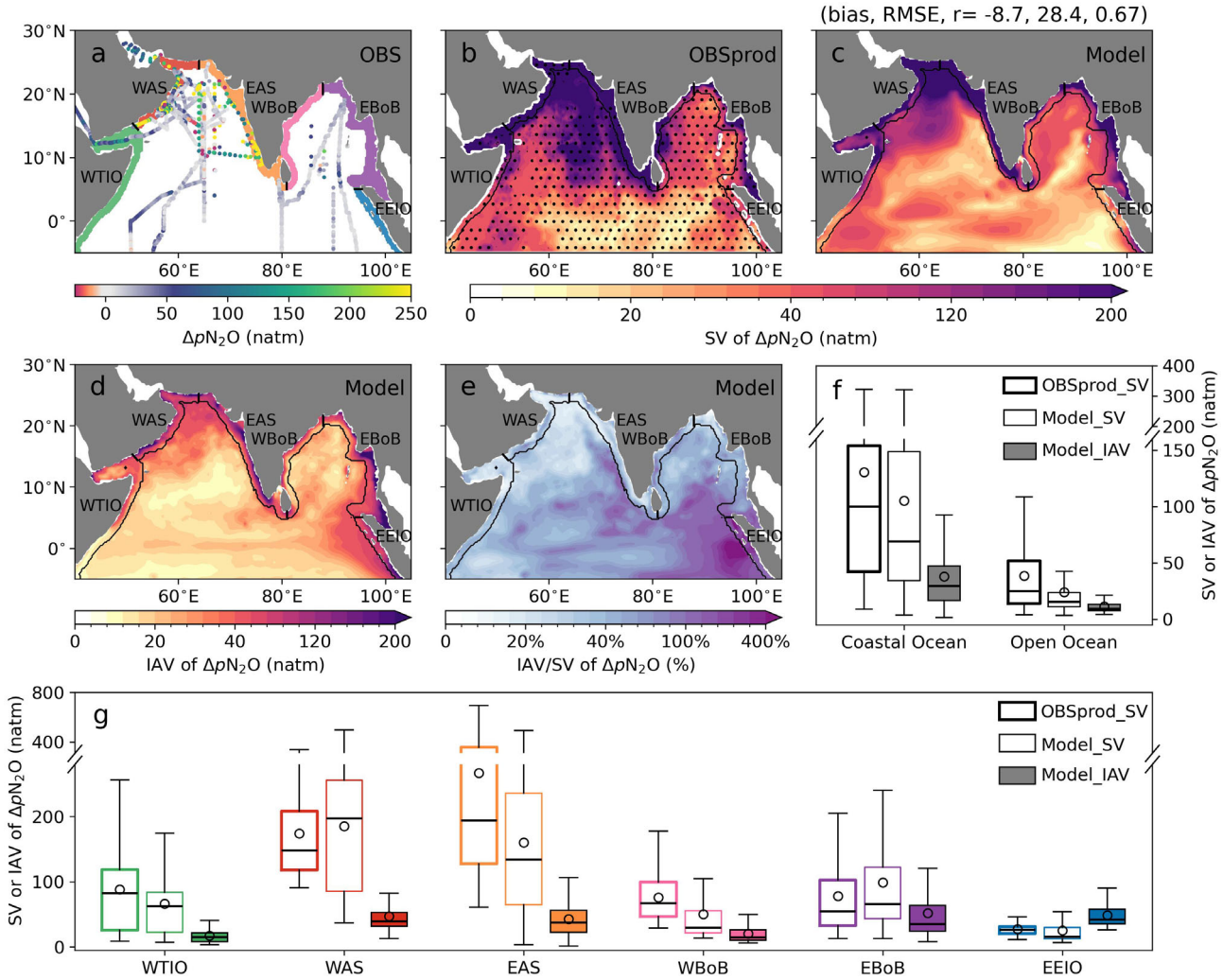

Fig. 1. Seasonal variability (SV) and interannual variability (IAV) in ΔpN_2O in the Indian Ocean north of 5°S. (**a**) Observed ΔpN_2O (OBS, Yang et al. 2020). Spatial pattern of ΔpN_2O seasonal variability from (**b**) gap filled observation-based product (Yang et al. 2020) and (**c**) the COBALTv2-N_2O model over 1981–2020, with their comparison indicated by the bias, root mean squared error (RMSE) and correlation coefficient (r). Stippling indicates regions of larger uncertainties in seasonal variability (*see* "Observation-based Data and Model Evaluation" section). (**d**) Interannual variability in the model and (**e**) relative magnitude compared to seasonal variability (in %). The solid black line in panels (**b**–**e**) is the boundary of coastal regions as defined in "Coastal regions" section. (**f**, **g**) Area-weighted ΔpN_2O seasonal variability in observation-based product (hollow box, bold) and model (hollow box, thin), and ΔpN_2O interannual variability in the model (filled box) with data points (dots) in (**f**) coastal and open oceans and (**g**) individual coastal regions. Coastal regions are shown in (**a**): western tropical Indian Ocean (WTIO, green), western Arabian Sea (WAS, red), eastern Arabian Sea (EAS, orange), western Bay of Bengal (WBoB, pink), eastern Bay of Bengal (EBoB, purple), and eastern equatorial Indian Ocean (EEIO, blue). Seasonal variability and IAV are estimated as $\pm$ 1 standard deviation (2σ, *see* "Seasonal and interannual variability" section). Boxplots show median, interquartile range, outliers (defined as outside of 1.5 times the interquartile range) and dots indicate regional mean (*see* Supporting Information Fig. S13 for individual data points).

23782242, 2026, 1, Downloaded from https://agupubs.onlinelibrary.wiley.com/doi/10.1002/lol2.70086 by Xiamen University, Wiley Online Library on [08/01/2026]. See the Terms and Conditions (https://onlinelibrary.wiley.com/terms-and-conditions) on Wiley Online Library for rules of use; OA articles are governed by the applicable Creative Commons License

increasing up to 20-fold during La Niña while declining by an order of magnitude during El Niño due to shifts in ocean circulation and N_2O production pathways (Babbin et al. 2020; Ji et al. 2018; Gluschankoff et al. 2023). The accumulated N_2O at deep depths by suppressed upwelling during El Niño years could find its way to the atmosphere in the following seasons (Ji et al. 2019), affecting the seasonality of N_2O emissions in the eastern tropical Pacific. The N_2O interannual variability and its influence on N_2O emissions remain poorly constrained, particularly in the northern Indian Ocean (Arya et al. 2024).

The coastal upwelling systems in the northern Indian Ocean are largely affected by monsoon-driven local winds or remotely forced coastal Kelvin waves (Vinayachandran et al. 2021; Pearson et al. 2022; McCreary et al. 1993; Suresh et al. 2016). Alongshore winds in the western Arabian Sea (WAS) and western Bay of Bengal (WBoB) favor upwelling during the summer monsoon and downwelling during the winter monsoon (Schott and McCreary 2001; Vinayachandran et al. 2021), while the seasonal succession of upwelling/downwelling Kelvin waves strongly affects the coastal eastern Bay of Bengal (EBoB) and eastern Arabian Sea (Supporting Information Fig. S2a,b; Text S1; Rao et al. 2010; Suresh et al. 2016). Indian Ocean Dipole modulates this seasonality by influencing the amplitude of coastal upwelling/downwelling and associated biogeochemical dynamics through remotely forced coastal Kelvin waves (Supporting Information Fig. S2c,d; Text S1; Pearson et al. 2022; Aparna et al. 2012; Suresh et al. 2018). Positive IOD triggers easterly wind anomalies that stimulate upwelling Kelvin waves in the equatorial Indian Ocean propagating counterclockwise along the rim of the Bay of Bengal and excite downwelling Kelvin waves near the tip of India and Sri Lanka propagating to the eastern Arabian Sea during summer/autumn (Rao et al. 2010; Suresh et al. 2018). Negative IOD reverses this coastal Kelvin wave-induced pattern, favoring downwelling in the Bay of Bengal and upwelling in the eastern Arabian Sea (Suresh et al. 2018; Pearson et al. 2022).

These modulations by upwelling/downwelling influence coastal ocean oxygen concentrations and potentially affect N_2O production, transport and emissions. For instance, downwelling during positive IOD increases oxygen concentration and prevents anoxia (Vallivattathillam et al. 2017; Arya et al. 2024; Pearson et al. 2022), which could potentially dampen N_2O production by denitrification and N_2O emissions in the eastern Arabian Sea. The basin-scale effect of IOD on N_2O emissions is however largely unconstrained. In this study, we examine the influence of interannual variability introduced by the IOD on the seasonality of ΔpN_2O (i.e., difference in partial pressure of N_2O between the ocean surface and the atmosphere that regulates emissions). We focus on the coastal ocean, which contributes approximately a third to the N_2O emissions in the northern Indian Ocean, despite covering only $\sim 20\%$ of its area (146 ± 92 of 426 ± 265 Gg N yr^{-1} in the observation-based product, annual mean $\pm$ seasonal variability, Yang et al. 2020). To this end, we use a regional ocean model of the Indian Ocean based on GFDL MOM6-COBALTv2 with a mechanistically-based N_2O cycling module covering the period of 1981–2020 (COBALTv2-N_2O, Zhao et al. 2025a). The drivers of the response to IOD and its impact on N_2O emissions are also discussed.

Materials and methods

Model configuration and simulations

We use a regional ocean model of the Indian Ocean (north of 30° S) based on the Modular Ocean Model version 6 (MOM6) at a resolution of 0.25° with 75 vertical hybrid z^*-isopycnal levels (Adcroft et al. 2019), coupled with a version of the Carbon, Ocean Biogeochemistry and Lower Trophics module 2 that incorporates N_2O cycling (COBALTv2-N_2O, Stock et al. 2020; Zhao et al. 2025a). The model was run from 1981 to 2020 after a 40-yr spin-up (repeating the forcing of the year 1981), using the hourly atmospheric forcing and river discharge from the 5th-generation ECMWF atmospheric reanalysis (ERA5, Hersbach et al. 2020) and monthly open boundary conditions from Ocean Reanalysis System 5 (ORAS5, Zuo et al. 2019) for temperature, salinity and tidal forcing. See details in Zhao et al. (2025a).

COBALTv2-N_2O simulates N_2O production during nitrification (parameterized with an oxygen-dependent yield following Nevison et al. (2003) and Ji et al. (2018)) and production/consumption via denitrification (parameterized as a function of temperature, oxygen, substrate and particulate organic matter following Bianchi et al. (2023) and McCoy et al. (2023)). Nitrous oxide air–sea flux and solubility are calculated based on Wanninkhof (2014) and Weiss and Price (1980). The open boundary conditions of N_2O are set constant based on observed profiles from MEMENTO database (Kock and Bange 2015). Biological production by nitrification (N_2O^{nitrif}) and denitrification (N_2O^{denit}), as well as transport across the model open boundaries or exchanged across the air-sea interface (N_2O^{bc}) were tracked. A comprehensive description of the N_2O module and tracer decomposition is provided in Zhao et al. (2025a).

Observation-based data and model evaluation

We use ocean surface ΔpN_2O monthly climatology from Yang et al. (2020), and define regions with large uncertainties where the maximum monthly ensemble spread (standard deviation) exceeds 75% of the ensemble mean seasonal variability. We use satellite-based daily sea-level anomaly from the Global Ocean Gridded SSALTO/DUACS Sea Surface Height L4 product (https://cds.climate.copernicus.eu/datasets/satellite-sea-level-global?tab=overview), monthly sea surface temperature (SST) from the Hadley Centre Global Sea Ice and Sea Surface Temperature dataset, version 1.1 (https://climatedataguide.ucar.edu/climate-data/sst-data-hadisst-v11, Rayner et al. 2003), and the National Oceanic and Atmospheric Administration (NOAA) Optimum Interpolation Sea Surface Temperature, version 2 (https://psl.noaa.gov/data/gridded/data.noaa.oisst.v2.html, Reynolds et al. 2002), and monthly net primary

23782242, 2026, 1, Downloaded from https://agupubs.onlinelibrary.wiley.com/doi/10.1002/lol2.70086 by Xiamen University, Wiley Online Library on [08/01/2026]. See the Terms and Conditions (https://onlinelibrary.wiley.com/terms-and-conditions) on Wiley Online Library for rules of use; OA articles are governed by the applicable Creative Commons License

productivity relying on the updated Carbon-based Production Model algorithm (https://orca.science.oregonstate.edu/index.php, Westberry et al. 2008). All were re-gridded to a resolution of 0.25° × 0.25°.

Spatial patterns of physical fields and biogeochemical dynamics have been comprehensively evaluated in Zhao et al. (2025a). Figure 1 shows that the model reproduces the observed patterns of ΔpN_2O seasonal variability (correlation coefficient $r = 0.67$, Fig. 1b,c; details in "Coastal to open ocean contrast in ΔpN_2O temporal variability" section). The model also reproduces the observed variations in the east/west SST gradient associated with IOD (Supporting Information Fig. S3), as well as the spatial and seasonal anomalies observed in response to IOD for sea-level anomaly ($r > 0.7$ except spring of negative IOD when $r = 0.5$) and net primary productivity ($r > \sim 0.3$; Supporting Information Figs. S4, S5).

Seasonal and interannual variability

Observational and simulated fields were detrended by removing the long-term linear trend over the 1981–2020 period. Seasonal variability was computed as ± 1 standard deviation (2σ) of monthly climatology. Deseasonalized interannual anomalies were computed by subtracting the monthly climatology followed by a centered 3-month moving average filter. Interannual variability was computed as ± 1 standard deviation (2σ) of deseasonalized interannual anomalies.

Indian Ocean Dipole phases were quantified following Pearson et al. (2022) using an observation-based merged Dipole Mode Index (Saji et al. 1999) spanning 1958–2020 from Pearson et al. (2022), and two additional Dipole Mode Index time series using monthly SST datasets from Hadley Centre Global Sea Ice and Sea Surface Temperature dataset, version 1.1 for 1870–2023 and NOAA Optimum Interpolation Sea Surface Temperature, version 2 for 1981–2023. Composites of IOD positive and negative phases were calculated by averaging June of each IOD year to May of the following year and subtracting the climatological mean for the same period.

Coastal regions

Results are shown for the northern Indian Ocean (defined here as north of 5°S), and coastal regions defined by the outer limit of ~ 150 km from shore or the 1000 m isobath, whichever is farther (Laruelle et al. 2017; Resplandy et al. 2024). Coastal sub-regions include the western tropical Indian Ocean (WTIO), WAS and eastern Arabian Sea (EAS, boundary at 64°E), WBoB and EBoB (boundary at 87°E) and eastern equatorial Indian Ocean (EEIO, Fig. 1a).

Results and discussion

Coastal to open ocean contrast in ΔpN_2O temporal variability

Seasonality and interannual variability in ΔpN_2O in the northern Indian Ocean show a strong coastal to open ocean contrast. ΔpN_2O seasonality is about three times larger in the coastal ocean than in the open ocean in both the observation-based product and the model (median and interquartile range of 100 [42–154] vs. 25 [14–52] natm in observation-based product and 69 [34–149] vs. 15 [11–24] natm in model, Fig. 1b,c,f). Across coastal regions, seasonality is highest in the WAS and EAS (median seasonality of ~ 150–200 natm), followed by the WTIO, WBoB and EBoB (~ 50–70 natm), while it is lowest in the EEIO (~ 25 natm, Fig. 1g). The model captures relatively well the magnitude of coastal variability, but tends to simulate lower seasonality in the EAS and WBoB (Fig. 1g) where large uncertainties in the observation-based ΔpN_2O, stemming from sparse in-situ observations, potentially lead to biases in the gap-filled seasonal variability of the observation-based product (stippled regions in Fig. 1b; Supporting Information Fig. S6). This low bias could also be attributable to an underestimation of simulated primary productivity and N_2O production in the winter monsoon due to a bias in the vertical supply of nutrients by mixing or fine-scale eddies in these regions (Zhao et al. 2025a).

The model indicates that ΔpN_2O interannual variability associated with IOD (the correlation between ΔpN_2O and Dipole Mode Index is significant with p-value < 0.05; Supporting Information Fig. S7) is also about three times larger in the coastal ocean than in the open ocean (30 [17–47] vs. 9 [8–13] natm, Fig. 1d,f). In contrast to the seasonality pattern, interannual variability is high in the EEIO, WAS, EAS, and EBoB (median of ~ 40 natm) and low in the WBoB and western tropical Indian Ocean (~ 15 natm, Fig. 1g). Interannual variability represents ~ 60% of seasonal variability basin-wide (Fig. 1f), but its importance relative to seasonal variability varies widely depending on the region (interannual-to-seasonal ratio, Fig. 1e). The relative contribution of interannual variability peaks in the EEIO where interannual variability exceeds seasonal variability and decreases westward and northward (Fig. 1e). Specifically, we note that the interannual-to-seasonal ratio decreases counter-clockwise from ~ 260% in the EEIO, to ~ 50% in the EBoB and WBoB, and to 20–30% in the coastal regions of the western basin (Fig. 1g), aligning with the generation of upwelling/downwelling Kelvin waves in the equatorial Indian Ocean and their propagation around the basin in response to IOD phases (Supporting Information Fig. S2; Han and Webster 2002; Aparna et al. 2012; Pearson et al. 2022) and the stronger seasonal variability in the Arabian Sea than the Bay of Bengal (Fig. 1g).

Asymmetric response of ΔpN_2O variability to IOD

Figure 2 shows the asymmetric response of ΔpN_2O to positive and negative IOD phases in autumn, when IOD peaks, and the following winter, when IOD still influences ocean physical and biogeochemical processes (Aparna et al. 2012; Suresh et al. 2018; Pearson et al. 2022). Positive IOD increases ΔpN_2O in the east of the basin (e.g., EEIO and EBoB) and decreases ΔpN_2O in the west of the basin and the southwest Bay of Bengal, particularly in the EAS (Fig. 2a,c). These

23782242, 2026, 1, Downloaded from https://aslopubs.onlinelibrary.wiley.com/doi/10.1002/lol2.70086 by Xiamen University, Wiley Online Library on [08/01/2026]. See the Terms and Conditions (https://onlinelibrary.wiley.com/terms-and-conditions) on Wiley Online Library for rules of use; OA articles are governed by the applicable Creative Commons License

anomalies tend to propagate counter-clockwise from autumn to winter (Fig. 2a,c). This is consistent with the propagation of upwelling Kelvin waves triggered in the equatorial Indian Ocean that would favor dampened seasonal downwelling and high primary productivity, as well as the downwelling Kelvin waves generated near the tip of India and Sri Lanka that would deepen the thermocline and reduce primary productivity (Supporting Information Figs. S2n,o, S4n,o, S5n,o, Rao et al. 2010; Suresh et al. 2018; Pearson et al. 2022). Negative IOD reverses this pattern, reducing ΔpN_2O in the eastern basin while enhancing it in the west (Fig. 2b,d). Notably, however, negative IOD is characterized by smaller anomalies by a factor of 2 than positive IOD, particularly in the EEIO and EBoB (about −20 vs. +55–75 natm). This asymmetric response to positive and negative IOD is consistent with the amplitude asymmetry of IOD events (Hong et al. 2008; Nakazato et al. 2021), which modulates the transport of N_2O from the subsurface that controls ΔpN_2O variability (*see* "IOD-driven changes in N_2O sources of ΔpN_2O" section).

The asymmetric response to positive and negative IOD influences ΔpN_2O seasonality, introducing an east–west seesaw pattern, most evident in the coastal ocean (Fig. 2e,f). In the east, positive IOD enhances seasonal variability by a factor of 5 in the EEIO (+59 natm in regional median) and by ∼ 90% in the EBoB (+57 natm), while negative IOD dampens it only by ∼ 5% in both regions (about −1 and − 4 natm, respectively, Fig. 3a,b). In the west, on the other hand, positive IOD reduces seasonality by ∼ 30% in the EAS (−34 natm), while negative IOD increases it by only 10% (+14 natm, Fig. 3c). This asymmetry in ΔpN_2O response to IOD likely introduces a bias in seasonal reconstructions based on observations. Indeed, available ΔpN_2O observations are biased toward positive IOD in the west (Arabian Sea) and negative IOD in the east (Bay of Bengal; Supporting Information Fig. S1b,d). This sampling bias potentially yields an underestimation of ΔpN_2O seasonality and of the associated emissions in both the east and the west of the basin.

Indian Ocean Dipole–driven changes in N_2O sources of ΔpN_2O

We further examine the drivers of ΔpN_2O seasonality and how they are influenced by the IOD asymmetric response. We focus on three coastal ocean regions with the strongest

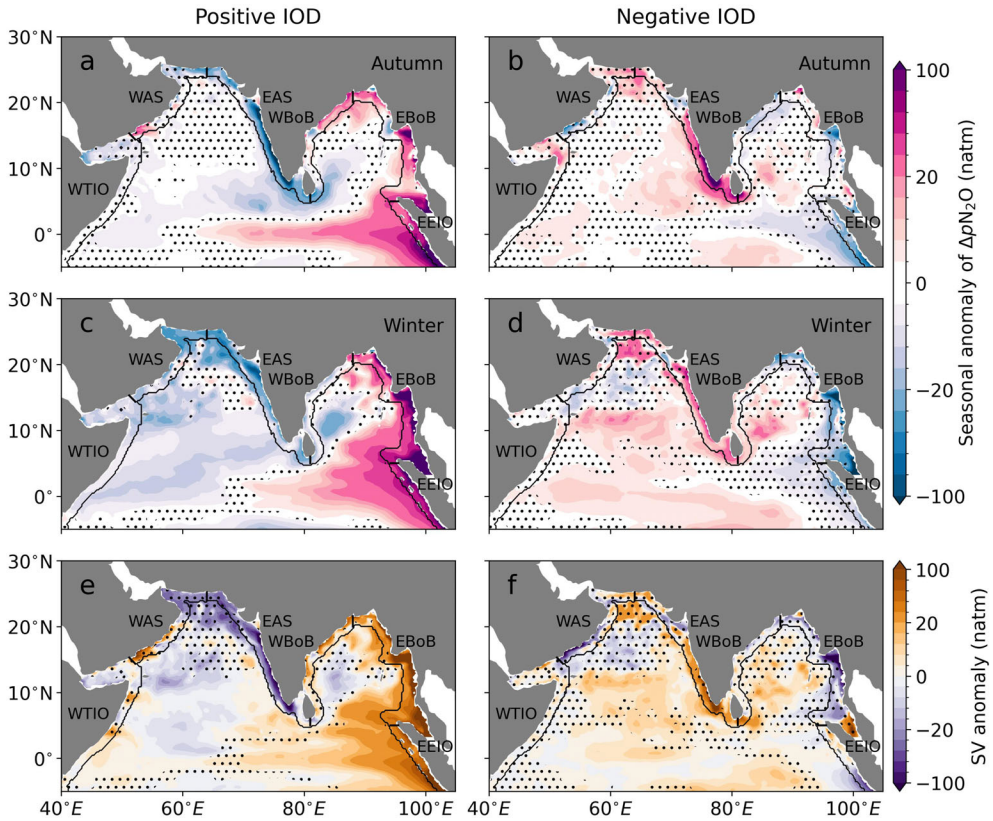

Fig. 2. The seasonal anomaly of the simulated ΔpN_2O in autumn (**a**, **b**) and winter (**c**, **d**) and anomalies in seasonal variability (SV, **e**, **f**) in positive Indian Ocean Dipole (IOD) (first column) and negative IOD (second column) phases. Autumn refers to September–October–November and winter refers to December–January–February. Stippling in (**a**, **b**), (**c**, **d**) and (**e**, **f**) indicates regions of insignificant autumn, winter, and annual anomaly, respectively, at the 95% confidence level from a two-tailed Student *t*-test. Seasonal variability is estimated as ± 1 standard deviation (2σ, *see* "Seasonal and interannual variability" section). The black lines indicate the boundary of the coastal and open oceans.

23782242, 2026, 1, Downloaded from https://aslopubs.onlinelibrary.wiley.com/doi/10.1002/lol2.70086 by Xiamen University, Wiley Online Library on [08/01/2026]. See the Terms and Conditions (https://onlinelibrary.wiley.com/terms-and-conditions) on Wiley Online Library for rules of use; OA articles are governed by the applicable Creative Commons License

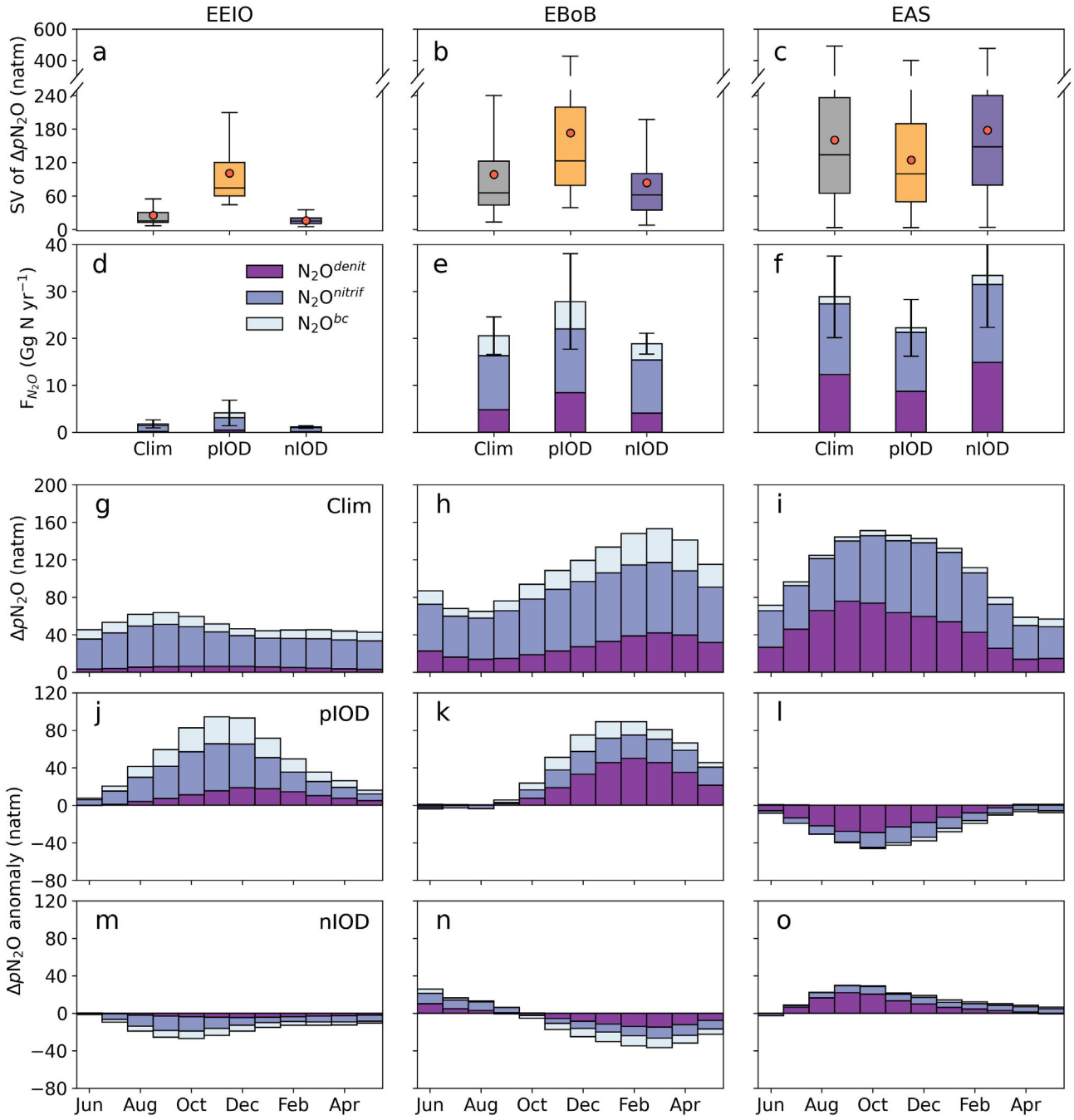

Fig. 3. Seasonal variability (SV) in ΔpN_2O (**a**–**c**) and annual mean emissions (F_{N_2O}, **d**–**f**) of N_2O produced by denitrification (N_2O^{denit}, dark purple), nitrification (N_2O^{nitrif}, blue) and transported from boundaries (N_2O^{bc}, light blue) in the coastal ocean regions of the eastern Arabian Sea (EAS), the eastern Bay of Bengal (EBoB), and the eastern equatorial Indian Ocean (EEIO) in climatological (Clim), positive IOD (pIOD) and negative IOD (nIOD) phases. Monthly climatological mean (Clim, **g**–**i**) and seasonal anomaly (**j**–**o**) in ΔpN_2O for N_2O^{denit}, N_2O^{nitrif} and N_2O^{bc} in these coastal ocean regions. Seasonal variability is estimated as ± 1 standard deviation (2σ, *see* "Seasonal and interannual variability" section). Boxplots in (**a**–**c**) show median, interquartile range, outliers (defined as outside of 1.5 times the interquartile range), red dots indicate regional mean and gray dots indicate data points (*see* Supporting Information Fig. S14 for individual data points). Error bars in (**d**–**f**) indicate ± 1 standard deviation of total N_2O emissions.

responses of ΔpN_2O variability to IOD, but distinct interannual-to-seasonal ratios: the EAS where seasonality exceeds interannual variability, the EBoB where both are comparable, and the EEIO where interannual variability exceeds seasonality (Figs. 1g, 2). Seasonal and interannual variations in ΔpN_2O are predominantly controlled by the transport of N_2O produced by

23782242, 2026, 1, Downloaded from https://agupubs.onlinelibrary.wiley.com/doi/10.1002/lol2.70086 by Xiamen University, Wiley Online Library on [08/01/2026]. See the Terms and Conditions (https://onlinelibrary.wiley.com/terms-and-conditions) on Wiley Online Library for rules of use; OA articles are governed by the applicable Creative Commons License

nitrification (N_2O^{nitrif}, typically at depths of 40–120 m) or denitrification in waters surrounding the oxygen minimum zones (N_2O^{denit}, typically at depths of 100–600 m, Fig. 3g–i). In contrast, contributions from N_2O production at the surface and from N_2O transport across the model open boundaries including the air–sea interface (N_2O^{bc}) are minor (Fig. 3g–i; Supporting Information Figs. S8–S10, refer to Zhao et al. (2025a) for a detailed pattern of N_2O production). ΔpN_2O seasonality is dominated by N_2O^{nitrif} in the EEIO (seasonal increase of ~ 15 natm), whereas it is controlled roughly equally by N_2O^{denit} and N_2O^{nitrif} in the EBoB (~ 30 natm for each) and even dominated by N_2O^{denit} in the EAS (~ 60 natm, Fig. 3g–i). This difference is explained by the proximity of EAS and EBoB to the oxygen minimum zones where N_2O^{denit} is produced and laterally transported to coastal upwelling regions through subsurface circulation (Zhao et al. 2025a).

Indian Ocean Dipole affects the EEIO ΔpN_2O seasonality mainly through changes in N_2O^{nitrif}, whereas the impact in the EBoB and EAS is mainly through changes in N_2O^{denit} (Fig. 3j–o). The asymmetry between positive and negative IOD dictates the magnitude and sign of the response, but not the relative contributions from N_2O^{denit} and N_2O^{nitrif} in each region. In the EEIO, N_2O^{nitrif} contributes to nearly 50% of ΔpN_2O seasonal anomalies during both positive and negative IOD, while N_2O^{denit} (~ 20%) and N_2O^{bc} (~ 30%) explain the remaining (Fig. 3j,m). In the EAS and EBoB, N_2O^{denit} accounts for ~ 55% and ~ 40–50% of ΔpN_2O seasonal anomalies, respectively, exceeding the contribution of N_2O^{nitrif} (~ 35% and ~ 20–30%, respectively) during both IOD phases. As a result, ΔpN_2O seasonality shifts from being dominated by N_2O^{nitrif} during negative phases to being dominated by N_2O^{denit} during positive phases in the EBoB (roughly half/half during non-IOD years, Fig. 3k,n), and from being equally controlled by N_2O^{nitrif} and N_2O^{denit} during positive IOD to a stronger dominance of N_2O^{denit} during negative IOD than during non-IOD years in the EAS (Fig. 3l,o). This shift toward a stronger contribution of N_2O^{denit} produced deeper in the water column during negative (positive) IOD in the EAS (EBoB) is consistent with the enhanced coastal upwelling (Supporting Information Fig. S4, Pearson et al. 2022). Net N_2O production in the surface mixed layer is much smaller than N_2O transport into the surface mixed layer (Supporting Information Fig. S8) and the changes in production are not only smaller by an order of magnitude than the changes in transport, but vary in the opposite direction during both IOD phases. Therefore, changes in N_2O production are a minor contribution to ΔpN_2O seasonal anomalies (Supporting Information Figs. S9, S10). Since our model does not include N_2O input from rivers and cannot resolve physical and biogeochemical processes in estuaries, the impact of IOD-driven changes in river discharge on ΔpN_2O seasonal anomalies cannot be well constrained in this study.

Impact on N_2O emissions

Indian Ocean Dipole–driven changes in ΔpN_2O seasonality influence local N_2O emissions. Positive IOD enhances annual N_2O emissions, relative to climatological mean, by ~ 130% and ~ 35% in the EEIO and EBoB regions (~ 10.0 mg N m^{-2} yr^{-1} for each), but reduces them by ~ 25% in the EAS (−11.6 mg N m^{-2} yr^{-1}, Fig. 3d–f). In contrast, negative IOD reduces N_2O emissions by ~ 40% and ~ 10% in the EEIO and EBoB (−3.0 and − 2.4 mg N m^{-2} yr^{-1}), but increases them by ~ 15% in the EAS (+7.9 mg N m^{-2} yr^{-1}, Fig. 3d–f). These changes in annual emissions are associated with changes in emission seasonal amplitude, following seasonal anomalies in ΔpN_2O and shifts in N_2O sources (*see* "IOD-driven changes in N_2O sources of ΔpN_2O" section). For instance, in the EEIO, N_2O emission seasonality increases by about a factor of 3 during positive IOD and decreases by about two-thirds during negative IOD due mainly to changes in N_2O^{nitrif} (Fig. 3d). In contrast, in the EAS N_2O emission seasonality weakens (intensifies) by ~ 30% during positive (negative) IOD due primarily to changes in N_2O^{denit} (Fig. 3f). We note that IOD-driven changes in winds have a relatively small influence on N_2O emissions, but they decouple the peak in N_2O emission anomalies in early autumn from the peak in ΔpN_2O anomalies in late autumn/early winter in the EEIO and EAS (Supporting Information Figs. S9d–f, S10d–f, S11).

Overall, changes in N_2O emissions largely compensate between western and eastern Indian Ocean regions but the western anomalies control the sign of change, leading to less emissions during positive IOD and more emissions during negative IOD. As a result, total annual N_2O emissions in the northern Indian Ocean only change by $-2.4\% \pm 2.6\%$ (-8.0 ± 8.5 Gg N yr^{-1}, annual mean ± seasonal variability) and $4.1\% \pm 4.4\%$ (13.5 ± 14.3 Gg N yr^{-1}) during positive and negative IOD, respectively. These estimates might be biased low due to the underestimation of simulated ΔpN_2O in the western regions where N_2O emissions are relatively high (e.g., the eastern Arabian Sea, *see* "Coastal to open ocean contrast in ΔpN_2O temporal variability" section). However, during strong positive IOD, known to amplify the east–west contrast of positive IOD (e.g., years of 1994, 1997, and 2019, Pearson et al. 2022; Wang et al. 2020), eastern anomalies become much stronger and exceed the western anomaly (e.g., increasing to ~ 220% in the EEIO and ~ 50% in the EBoB), shifting the total N_2O emission anomalies in the northern Indian Ocean from negative to positive (11.0 ± 13.0 Gg N yr^{-1}; Supporting Information Fig. S12). Total emission anomalies during strong positive IOD therefore resemble negative IOD and not other weaker positive IOD. As the frequency of strong positive IOD is projected to rise in the future (Cai et al. 2021; Wang et al. 2024), this could lead to a scenario where all IOD phases contribute to increased N_2O emissions.

23782242, 2026, 1, Downloaded from https://aslopubs.onlinelibrary.wiley.com/doi/10.1002/lol2.70086 by Xiamen University, Wiley Online Library on [08/01/2026]. See the Terms and Conditions (https://onlinelibrary.wiley.com/terms-and-conditions) on Wiley Online Library for rules of use; OA articles are governed by the applicable Creative Commons License

Summary and implications

The main findings of this study are:

- *Coastal to open ocean contrast*—Seasonal and interannual variability in ΔpN_2O are three times greater in the coastal than open Indian Ocean.
- *Asymmetric response to IOD*—Positive IOD enhances ΔpN_2O seasonality by a factor 2 to 5 in the east and reduces it by $\sim$ 30% in the west, while negative IOD reverses this pattern with weaker changes (< 10%).
- *Heterogeneous changes in N_2O sources*—The response of ΔpN_2O seasonality to IOD arises from the transport of N_2O from the subsurface by nitrification in the EEIO and denitrification in the EAS and EBoB.
- *Compensating east–west N_2O emissions*—Total annual N_2O emissions only change by −2% to 4% during IOD in the northern Indian Ocean, despite local changes of −40% to 130% in the EEIO.

Potential caveats and future implications include:

- The underestimation of simulated ΔpN_2O in the eastern Arabian Sea might lead to a low bias in the response of N_2O seasonality to IOD since the western anomalies control the sign of IOD-driven changes.
- The asymmetric response to IOD suggests an underestimation of reconstructed ΔpN_2O seasonality and associated emissions based on observations due to the sampling bias. A balanced coverage of coastal regions (e.g., the Bay of Bengal) across seasons and IOD phases for N_2O observations is thus needed to better constrain N_2O emissions.
- Despite being small compared to global ocean N_2O emissions, IOD-driven changes in N_2O emissions in the northern Indian Ocean are expected to be a hotspot of global ocean N_2O interannual variability.

Author Contributions

Yangyang Zhao and Laure Resplandy designed the study. Yangyang Zhao, Fan Yang, and Xianhui Sean Wan developed the methodology. Yangyang Zhao conducted data analysis, created figures, and drafted the original manuscript, with contributions from Laure Resplandy, Fan Yang, and Calla Marchetti. Laure Resplandy supervised the study, data processing, and interpretation. Yangyang Zhao, Laure Resplandy, Fan Yang, Xianhui Sean Wan, Calla Marchetti, and Bess Ward contributed to manuscript review and editing. Laure Resplandy and Bess Ward secured funding.

Acknowledgments

This work was supported by the NOAA Climate Program Office Award No. NA21OAR4310119, and the High Meadows Environmental Institute Climate, Chemistry and Life in the Indian Ocean Initiative and the NSF CAREER Award No. 2042672. The authors thank Nicolas Gruber from ETH, Switzerland, and Daniele Bianchi from University of California, Los Angels, USA, for their constructive suggestions, and Enhui Liao from Shanghai Jiaotong University, China, and Wenchang Yang from Princeton University, USA, for their help in data processing.

Data Availability Statement

The MOM6-COBALTv2-N_2O model used to generate the simulation is described in Zhao et al. (2025a) and is reproducible using the model code and forcing files available at the Zenodo repository https://doi.org/10.5281/zenodo.14489075 (Zhao et al. 2024a) and https://doi.org/10.5281/zenodo.14490932 (Zhao et al. 2024b). The model outputs analyzed in this study and observation-based data used for model evaluation are available at https://doi.org/10.5281/zenodo.17306281 (Zhao et al. 2025b).

References

Adcroft, A., W. Anderson, V. Balaji, et al. 2019. "The GFDL Global Ocean and Sea Ice Model OM4.0: Model Description and Simulation Features." *Journal of Advances in Modeling Earth Systems* 11, no. 10: 3167–3211. https://doi.org/10.1029/2019MS001726.

Aparna, S. G., J. P. McCreary, D. Shankar, and P. N. Vinayachandran. 2012. "Signatures of Indian Ocean Dipole and El Niño–Southern Oscillation Events in Sea Level Variations in the Bay of Bengal." *Journal of Geophysical Research. Oceans* 117, no. C10: 434–439. https://doi.org/10.1029/2012JC008055.

Arya, K. S., T. R. Gireeshkumar, E. R. Vignesh, et al. 2024. "Distribution and Sea-to-Air Fluxes of Nitrous Oxide and Methane From a Seasonally Hypoxic Coastal Zone in the Southeastern Arabian Sea." *Marine Pollution Bulletin* 205, no. August: 116614. https://doi.org/10.1016/j.marpolbul.2024.116614.

Babbin, A. R., E. L. Boles, J. Mühle, and R. F. Weiss. 2020. "On the Natural Spatio-Temporal Heterogeneity of South Pacific Nitrous Oxide." *Nature Communications* 11, no. 1: 3672. https://doi.org/10.1038/s41467-020-17509-6.

Bianchi, D., D. McCoy, and S. Yang. 2023. "Formulation, Optimization, and Sensitivity of NitrOMZv1.0, a Biogeochemical Model of the Nitrogen Cycle in Oceanic Oxygen Minimum Zones." *Geoscientific Model Development* 16, no. 12: 3581–3609. https://doi.org/10.5194/gmd-16-3581-2023.

Cai, W., K. Yang, L. Wu, et al. 2021. "Opposite Response of Strong and Moderate Positive Indian Ocean Dipole to Global Warming." *Nature Climate Change* 11, no. 1: 27–32. https://doi.org/10.1038/s41558-020-00943-1.

Gluschankoff, N., A. E. Santoro, C. Buchwald, and K. L. Casciotti. 2023. "Shifts in the Isotopic Composition of Nitrous Oxide Between El Niño and La Niña in the Eastern Tropical South Pacific." *Global Biogeochemical*

23782242, 2026, 1, Downloaded from https://agupubs.onlinelibrary.wiley.com/doi/10.1002/lo2.70086 by Xiamen University, Wiley Online Library on [08/01/2026]. See the Terms and Conditions (https://onlinelibrary.wiley.com/terms-and-conditions) on Wiley Online Library for rules of use; OA articles are governed by the applicable Creative Commons License

Cycles 37, no. 10: e2023GB007959. https://doi.org/10.1029/2023GB007959.

Han, W., and P. J. Webster. 2002. "Forcing Mechanisms of Sea Level Interannual Variability in the Bay of Bengal." *Journal of Physical Oceanography*. *Journal of Physical Oceanography* 32, no. 1: 216–239. https://doi.org/10.1175/1520-0485(2002)032%253C0216:FMOSLI%253E2.0.CO;2.

Hersbach, H., B. Bell, P. Berrisford, et al. 2020. "The ERA5 Global Reanalysis." *Quarterly Journal of the Royal Meteorological Society* 146, no. 730: 1999–2049. https://doi.org/10.1002/qj.3803.

Hong, C.-C., T. Li, LinHo, and J.-S. Kug. 2008. "Asymmetry of the Indian Ocean Dipole. Part I: Observational Analysis." *Journal of Climate* 21, no. 18: 4834–4848. https://doi.org/10.1175/2008JCLI2222.1.

Ji, Q., M. A. Altabet, H. W. Bange, et al. 2019. "Investigating the Effect of El Niño on Nitrous Oxide Distribution in the Eastern Tropical South Pacific." *Biogeosciences* 16, no. 9: 2079–2093. https://doi.org/10.5194/bg-16-2079-2019.

Ji, Q., E. Buitenhuis, P. Suntharalingam, J. L. Sarmiento, and B. B. Ward. 2018. "Global Nitrous Oxide Production Determined by Oxygen Sensitivity of Nitrification and Denitrification." *Global Biogeochemical Cycles* 32, no. 12: 1790–1802. https://doi.org/10.1029/2018GB005887.

Kock, A., and H. W. Bange. 2015. "Counting the Ocean's Greenhouse Gas Emissions." *Eos, Transactions of the American Geophysical Union* 96, no. 3: 10–13. https://doi.org/10.1029/2015E0023665.

Lal, S., and P. K. Patra. 1998. "***Variabilities in the Fluxes and Annual Emissions of Nitrous Oxide From the Arabian Sea." *Global Biogeochemical Cycles* 12, no. 2: 321–327. https://doi.org/10.1029/98GB00444.

Laruelle, G. G., P. Landschützer, N. Gruber, J.-L. Tison, B. Delille, and P. Regnier. 2017. "Global High-Resolution Monthly pCO_2 Climatology for the Coastal Ocean Derived From Neural Network Interpolation." *Biogeosciences* 14, no. 19: 4545–4561. https://doi.org/10.5194/bg-14-4545-2017.

McCoy, D., P. Damien, D. Clements, S. Yang, and D. Bianchi. 2023. "Pathways of Nitrous Oxide Production in the Eastern Tropical South Pacific Oxygen Minimum Zone." *Global Biogeochemical Cycles* 37, no. 7: e2022GB007670. https://doi.org/10.1029/2022GB007670.

McCreary, J. P., P. K. Kundu, and R. L. Molinari. 1993. "A Numerical Investigation of Dynamics, Thermodynamics and Mixed-Layer Processes in the Indian Ocean." *Progress in Oceanography* 31, no. 3: 181–244. https://doi.org/10.1016/0079-6611(93)90002-U.

Nakazato, M., S. Kido, and T. Tozuka. 2021. "Mechanisms of Asymmetry in Sea Surface Temperature Anomalies Associated with the Indian Ocean Dipole Revealed by Closed Heat Budget." *Scientific Reports* 11, no. 1: 22546. https://doi.org/10.1038/s41598-021-01619-2.

Nevison, C., J. H. Butler, and J. W. Elkins. 2003. "Global Distribution of N_2O and the ΔN_2O-AOU Yield in the Subsurface Ocean." *Global Biogeochemical Cycles* 17, no. 4: 1119. https://doi.org/10.1029/2003GB002068.

Pearson, J., L. Resplandy, and M. Poupon. 2022. "Coastlines at Risk of Hypoxia From Natural Variability in the Northern Indian Ocean." *Global Biogeochemical Cycles* 36, no. 6: e2021GB007192. https://doi.org/10.1029/2021GB007192.

Prather, M. 2001. "Atmospheric Chemistry and Greenhouse Gases." Climate Change 2001: The Scientific Basis. Contribution of Working Group I to the Third Assessment Report of the Intergovernmental Panel on Climate Change https://cir.nii.ac.jp/crid/1573950399987760512.

Rao, R. R., M. S. Girish Kumar, M. Ravichandran, A. R. Rao, V. V. Gopalakrishna, and P. Thadathil. 2010. "Interannual Variability of Kelvin Wave Propagation in the Wave Guides of the Equatorial Indian Ocean, the Coastal Bay of Bengal and the Southeastern Arabian Sea during 1993–2006." *Deep Sea Research Part I: Oceanographic Research Papers* 57, no. 1: 1–13. https://doi.org/10.1016/j.dsr.2009.10.008.

Rayner, N. A., D. E. Parker, E. B. Horton, et al. 2003. "Global Analyses of Sea Surface Temperature, Sea Ice, and Night Marine Air Temperature since the Late Nineteenth Century." *Journal of Geophysical Research: Atmospheres* 108, no. D14: 4407. https://doi.org/10.1029/2002JD002670.

Resplandy, L., A. Hogikyan, J. D. Müller, et al. 2024. "A Synthesis of Global Coastal Ocean Greenhouse Gas Fluxes." *Global Biogeochemical Cycles* 38, no. 1: e2023GB007803. https://doi.org/10.1029/2023GB007803.

Reynolds, R. W., N. A. Rayner, T. M. Smith, D. C. Stokes, and W. Wang. 2002. "An Improved in Situ and Satellite SST Analysis for Climate." *Journal of Climate* 15, no. 13: 1609–1625. https://doi.org/10.1175/1520-0442(2002)015%253C1609:AIISAS%253E2.0.CO;2.

Saji, N. H., B. N. Goswami, P. N. Vinayachandran, and T. Yamagata. 1999. "A Dipole Mode in the Tropical Indian Ocean." *Nature* 401, no. 6751: 360–363. https://doi.org/10.1038/43854.

Schott, F. A., and J. P. McCreary. 2001. "The Monsoon Circulation of the Indian Ocean." *Progress in Oceanography* 51, no. 1: 1–123. https://doi.org/10.1016/S0079-6611(01)00083-0.

Schott, F. A., S.-P. Xie, and J. P. McCreary Jr. 2009. "Indian Ocean Circulation and Climate Variability." *Reviews of Geophysics* 47, no. 1: RG1002. https://doi.org/10.1029/2007RG000245.

Stock, C. A., J. P. Dunne, S. Fan, et al. 2020. "Ocean Biogeochemistry in GFDL's Earth System Model 4.1 and Its Response to Increasing Atmospheric CO_2." *Journal of Advances in Modeling Earth Systems* 12, no. 10: e2019MS002043. https://doi.org/10.1029/2019MS002043.

Suresh, I., J. Vialard, T. Izumo, et al. 2016. "Dominant Role of Winds near Sri Lanka in Driving Seasonal Sea Level Variations along the West Coast of India." *Geophysical Research*

23782242, 2026, 1, Downloaded from https://agupubs.onlinelibrary.wiley.com/doi/10.1002/lol2.70086 by Xiamen University, Wiley Online Library on [08/01/2026]. See the Terms and Conditions (https://onlinelibrary.wiley.com/terms-and-conditions) on Wiley Online Library for rules of use; OA articles are governed by the applicable Creative Commons License

Letters 43, no. 13: 7028–7035. https://doi.org/10.1002/2016GL069976.

Suresh, I., J. Vialard, M. Lengaigne, T. Izumo, V. Parvathi, and P. M. Muraleedharan. 2018. "Sea Level Interannual Variability along the West Coast of India." *Geophysical Research Letters* 45, no. 22: 12440–12448. https://doi.org/10.1029/2018GL080972.

Tian, H., N. Pan, R. L. Thompson, et al. 2024. "Global Nitrous Oxide Budget (1980–2020)." *Earth System Science Data* 16, no. 6: 2543–2604. https://doi.org/10.5194/essd-16-2543-2024.

Tian, H., R. Xu, J. G. Canadell, et al. 2020. "A Comprehensive Quantification of Global Nitrous Oxide Sources and Sinks." *Nature* 586, no. 7828: 248–256. https://doi.org/10.1038/s41586-020-2780-0.

Vallivattathillam, P., S. Iyyappan, M. Lengaigne, et al. 2017. "Positive Indian Ocean Dipole Events Prevent Anoxia off the West Coast of India." *Biogeosciences* 14, no. 6: 1541–1559. https://doi.org/10.5194/bg-14-1541-2017.

Vinayachandran, P. N. M., Y. Masumoto, M. J. Roberts, et al. 2021. "Reviews and Syntheses: Physical and Biogeochemical Processes Associated with Upwelling in the Indian Ocean." *Biogeosciences* 18, no. 22: 5967–6029. https://doi.org/10.5194/bg-18-5967-2021.

Wang, G., W. Cai, A. Santoso, et al. 2024. "The Indian Ocean Dipole in a Warming World." *Nature Reviews Earth & Environment* 5, no. 8: 588–604. https://doi.org/10.1038/s43017-024-00573-7.

Wang, G., W. Cai, K. Yang, A. Santoso, and T. Yamagata. 2020. "A Unique Feature of the 2019 Extreme Positive Indian Ocean Dipole Event." *Geophysical Research Letters* 47, no. 18: e2020GL088615. https://doi.org/10.1029/2020GL088615.

Wanninkhof, R. 2014. "Relationship between Wind Speed and Gas Exchange over the Ocean Revisited." *Limnology and Oceanography: Methods* 12, no. 6: 351–362. https://doi.org/10.4319/lom.2014.12.351.

Weiss, R. F., and B. A. Price. 1980. "Nitrous Oxide Solubility in Water and Seawater." *Marine Chemistry* 8, no. 4: 347–359. https://doi.org/10.1016/0304-4203(80)90024-9.

Westberry, T., M. J. Behrenfeld, D. A. Siegel, and E. Boss. 2008. "Carbon-Based Primary Productivity Modeling with Vertically Resolved Photoacclimation." *Global Biogeochemical Cycles* 22, no. 2: GB2024. https://doi.org/10.1029/2007GB003078.

Yang, S., B. X. Chang, M. J. Warner, et al. 2020. "Global Reconstruction Reduces the Uncertainty of Oceanic Nitrous Oxide Emissions and Reveals a Vigorous Seasonal Cycle." *Proceedings of the National Academy of Sciences* 117, no. 22: 11954–11960. https://doi.org/10.1073/pnas.1921914117.

Zhao, Y., L. Resplandy, X. S. Wan, F. Yang, E. Liao, and B. Ward. 2024*a*. "Model Input for 'Decoupling of N_2O Production and Emissions in the Northern Indian Ocean.'" Version v1. Zenodo https://doi.org/10.5281/zenodo.14490932.

Zhao, Y., L. Resplandy, X. S. Wan, F. Yang, E. Liao, and B. Ward. 2024*b*. "Model Source Code for 'Decoupling of N_2O Production and Emissions in the Northern Indian Ocean.'" Version v1. Zenodo https://doi.org/10.5281/zenodo.14489075.

Zhao, Y., L. Resplandy, X. S. Wan, F. Yang, E. Liao, and B. Ward. 2025*a*. "Decoupling of N_2O Production and Emissions in the Northern Indian Ocean." *Global Biogeochemical Cycles* 39, no. 4: e2024GB008481. https://doi.org/10.1029/2024GB008481.

Zhao, Y., L. Resplandy, F. Yang, X. S. Wan, C. Marchetti, and B. Ward. 2025*b*. "Model Output and Evaluation for 'The Imprint of Indian Ocean Dipole on Nitrous Oxide Dynamics.'" Version v2. Zenodo https://doi.org/10.5281/zenodo.17306281.

Zuo, H., M. A. Balmaseda, S. Tietsche, K. Mogensen, and M. Mayer. 2019. "The ECMWF Operational Ensemble Reanalysis–Analysis System for Ocean and Sea Ice: A Description of the System and Assessment." *Ocean Science* 15, no. 3: 779–808. https://doi.org/10.5194/os-15-779-2019.

Supporting Information

Additional Supporting Information may be found in the online version of this article.

Submitted 04 June 2025
Revised 22 November 2025
Accepted 28 November 2025

23782242, 2026, 1, Downloaded from https://agupubs.onlinelibrary.wiley.com/doi/10.1002/lol2.70086 by Xiamen University, Wiley Online Library on [08/01/2026]. See the Terms and Conditions (https://onlinelibrary.wiley.com/terms-and-conditions) on Wiley Online Library for rules of use; OA articles are governed by the applicable Creative Commons License